



Title	Cirrus cloud appearance in a volcanic aerosol layer around the tropical cold point tropopause over Biak, Indonesia, in January 2011
Author(s)	Shibata, T.; Hayashi, M.; Naganuma, A.; Hara, N.; Hara, K.; Hasebe, F.; Shimizu, K.; Komala, N.; Inai, Y.; Vömel, H.; Hamdi, S.; Iwasaki, S.; Fujiwara, M.; Shiotani, M.; Ogino, S.-Y.; Nishi, N.
Citation	Journal of Geophysical Research: Atmospheres, 117(D11), n/a-n/a <a href="https://doi.org/10.1029/2011JD017029">https://doi.org/10.1029/2011JD017029</a>
Issue Date	2012
Doc URL	<a href="http://hdl.handle.net/2115/64770">http://hdl.handle.net/2115/64770</a>
Type	article
File Information	Shibata_et_al-2012-Journal_of_Geophysical_Research__Atmospheres_(1984-2012).pdf



[Instructions for use](#)

# Cirrus cloud appearance in a volcanic aerosol layer around the tropical cold point tropopause over Biak, Indonesia, in January 2011

T. Shibata,<sup>1</sup> M. Hayashi,<sup>2</sup> A. Naganuma,<sup>3</sup> N. Hara,<sup>2</sup> K. Hara,<sup>2</sup> F. Hasebe,<sup>4</sup> K. Shimizu,<sup>4</sup> N. Komala,<sup>5</sup> Y. Inai,<sup>1,6</sup> H. Vömel,<sup>7</sup> S. Hamdi,<sup>5</sup> S. Iwasaki,<sup>8</sup> M. Fujiwara,<sup>4</sup> M. Shiotani,<sup>9</sup> S.-Y. Ogino,<sup>10</sup> and N. Nishi<sup>11</sup>

Received 17 October 2011; revised 23 April 2012; accepted 25 April 2012; published 7 June 2012.

[1] An aerosol layer was found 1–2 km around the tropical cold point tropopause by observations using ground-based lidar and balloon-borne optical particle counters (OPC) over Biak, Indonesia, in January 2011. The layer was observed throughout the survey period from 6 to 13 January. The backscattering coefficient of the layer was about 5 times larger than that of the background aerosols. The lidar-observed depolarization ratio of the layer was very low, and the wavelength dependence of the backscattering coefficients of the layer was similar to that of stratospheric aerosols. A layer of the particles at the size of the accumulation mode was also observed by an OPC at ambient temperature, but the particles were volatile at 200°C. These properties indicate that the aerosol layer was composed of liquid phase aqueous sulfuric acid solution particles and probably originated from a volcanic eruption. It was observed by lidar that a thin cirrus cloud layer appeared within this aerosol layer. Backward trajectory analysis and satellite-observed equivalent blackbody temperature indicate that the cirrus cloud layer probably formed in situ. The estimated upper limit of the number concentration of cloud particles was  $10^5 \text{ m}^{-3}$ . The number concentration of the volatile aerosol particles ( $\sim 3 \times 10^6 \text{ m}^{-3}$ ) was 30 times larger than this upper limit. This upper limit, however, is comparable to the aerosol particle concentration observed by the OPC at 200°C. These results are consistent with the cirrus cloud formation with solid sulfate particles in tropical upper troposphere suggested by previous studies.

**Citation:** Shibata, T., et al. (2012), Cirrus cloud appearance in a volcanic aerosol layer around the tropical cold point tropopause over Biak, Indonesia, in January 2011, *J. Geophys. Res.*, 117, D11209, doi:10.1029/2011JD017029.

## 1. Introduction

[2] Stratospheric water vapor concentration is considered to be controlled mainly by the dehydration processes in the cold tropical tropopause region and by the oxidation of methane [Brewer, 1949; Fueglistaler et al., 2009]. Dehydration is the process of phase transfer from water vapor to ice cloud particles and the subsequent removal of those particles including the water vapor by gravitational sedimentation from the air parcel. Despite a great deal of effort being concentrated on this issue, the tropical dehydration process and especially the microphysical mechanisms of the ice formation are still unclear [e.g., Hasebe et al., 2007]. Lower stratospheric water vapor increased from 1980 to 2000 and suddenly decreased after 2000 [Oltmans and Hofmann, 1995; Fujiwara et al., 2010; Hurst et al., 2011]. The mechanism of these variations is still not well understood. However, the mechanism is important because the lower stratospheric water vapor or dehydration in the tropical tropopause region has a significant effect on global climate at ground level, since the radiation budget is changed due to

<sup>1</sup>Graduate School of Environmental Studies, Nagoya University, Nagoya, Japan.

<sup>2</sup>Faculty of Science, Fukuoka University, Fukuoka, Japan.

<sup>3</sup>Graduate School of Science, Fukuoka University, Fukuoka, Japan.

<sup>4</sup>Faculty of Environmental Earth Science, Hokkaido University, Sapporo, Japan.

<sup>5</sup>Lembaga Penerbangan dan Antariksa Nasional, Bandung, Indonesia.

<sup>6</sup>Now at Graduate School of Science, Tohoku University, Sendai, Japan.

<sup>7</sup>Meteorologisches Observatorium Lindenberg, Deutscher Wetterdienst, Lindenberg, Germany.

<sup>8</sup>National Defense Academy, Yokosuka, Japan.

<sup>9</sup>Research Institute for Sustainable Humanosphere, Kyoto University, Uji, Japan.

<sup>10</sup>Japan Agency for Marine-Earth Science and Technology, Yokosuka, Japan.

<sup>11</sup>Graduate School of Science, Kyoto University, Kyoto, Japan.

Corresponding author: T. Shibata, Graduate School of Environmental Studies, Nagoya University, Nagoya 464-8601, Japan. (shibata\_takashi@nagoya-u.jp)

variation in the amount of water vapor in the lower stratosphere [Solomon *et al.*, 2010].

[3] Since the tropical tropopause region has both tropospheric and stratospheric properties, it is defined as the tropical tropopause layer (TTL) [Highwood and Hoskins, 1998; Fueglistaler *et al.*, 2009]. The ice particles in TTL are formed from ambient aerosol particles as ice cloud particles in other latitudes and/or altitudes in the atmosphere. Although there is long history of studies on the nucleation process of ice cloud particles in the atmosphere [e.g., Pruppacher and Klett, 1978], new ice formation processes are still being proposed [e.g., Koop *et al.*, 2000; Murray *et al.*, 2005; Zobrist *et al.*, 2008]. The homogeneous nucleation ratio of ice within solution droplet aerosol particles is relevant for the estimation of ice particle formation in the tropical upper troposphere [Koop *et al.*, 2000]. However, the observed number concentration of cirrus cloud particles is a few orders of magnitude smaller than the number concentration predicted by homogeneous nucleation [Krämer *et al.*, 2009; Jensen *et al.*, 2010]. Jensen *et al.* [2010] suggested that the ice particle formation is not likely to occur due to the homogeneous nucleation in the solution droplet aerosol particles, but is much more likely to occur due to the presence of solid particles such as ammonium sulfate. Laboratory experiments support this suggestion that externally mixed ammonium sulfate particles work well as the ice nuclei at lower supersaturation [Wise *et al.*, 2010; Baustian *et al.*, 2010], but this heterogeneous nucleation has not been confirmed by reported field observations.

[4] The authors are conducting a project named “soundings of ozone and water in the equatorial region” (SOWER) to clarify the dehydration processes in the tropical upper troposphere at several western tropical Pacific sites [Hasebe *et al.*, 2007; Fujiwara *et al.*, 2010]. For the observations of the SOWER project we have been using a cryogenic frost-point hygrometer (CFH) and depolarization lidar at a single wavelength (532 nm) [Vömel *et al.*, 2007; Shibata *et al.*, 2007]. A lidar system was installed to observe cirrus clouds and their relation with water vapor at Bandung, Indonesia (6.90°S, 107.60°E) in 2003 [Shibata *et al.*, 2007] and was later moved to Biak, Indonesia (1.17°S, 136.06°E), where it has been operated since January 2006. During the survey in January 2011, in addition to the above mentioned instruments, we used balloon borne optical particle counters (OPC) and added a detector for the wavelength at 1064 nm to the lidar system.

[5] In our SOWER survey in January 2011, we found an aerosol layer around the cold point tropopause (CPT) and observed an event in which a layer of cirrus clouds formed within the aerosol layer. It is shown in this paper that the aerosol layer probably originated from a volcanic eruption. This event of the cirrus cloud formation will be a good additional test case for investigating whether the aqueous sulfuric acid aerosol particles from the volcanic origin work as the above mentioned ice nuclei [e.g., Sassen, 1992; Jensen and Toon, 1992]. The new instruments and improved lidar system were useful for detecting the cirrus cloud formation in the aerosol layer.

[6] The observation site and instruments are described in section 2, observational results are shown in section 3, and

their implications and the errors of lidar observed parameters are discussed in section 4.

## 2. Observations

### 2.1. Observation Site

[7] The SOWER survey was conducted at four observation sites in the tropical western Pacific region. The results shown in this paper were obtained at Biak, Indonesia. Biak is a city on the southern coast of Biak island, north of New Guinea. The observatory at Biak belongs to Lembaga Penerbangan dan Antariksa Nasional (LAPAN; National Institute of Aeronautics and Space Indonesia) for the observation of ionosphere. The observatory is about 2 km north of the coastline and about 50 m above sea level, and the lidar system is installed in one of its rooms. Balloon borne OPC and CFH are launched in the area of the site, and radio receivers for balloon telemetry are also installed at the observatory.

[8] The meteorological condition in January 2011 was as follows: Since typical La Nina condition prevailed in January 2011, the convective activity averaged in January was above normal to the west of Biak but rather close to the normal value around Biak. In the context of variability with intraseasonal time scale including Madden-Julian Oscillation, convective activity was also high to the west of Biak and rather low near Biak. As a result, cloud amount at Biak during the observational period was lower than in normal years. However, cirrus clouds in the upper troposphere were observed by lidar as frequently as in previous years, or cirrus clouds were observed almost continuously in the upper troposphere because of higher sensitivity of the ground based lidar.

### 2.2. Mie Depolarization Lidar

[9] The lidar system installed in Biak is a Nd:YAG laser-based Mie depolarization lidar. After a silicon avalanche photodiode (APD) detector to detect the signal at 1064 nm was added to the lidar at the beginning of the survey, the backscattering coefficient was observed at the wavelengths of the fundamental (1064 nm) and second harmonic generations (532 nm) of the laser. The laser beam is linearly polarized. The depolarization ratio was observed at the wavelength of 532 nm, although the wavelength at 1064 nm was not used for the depolarization measurements. The lidar data were integrated for each of the 600 laser shots (1 min) and for each 30 m vertical interval using 12 bit transient recorders. After taking a 5 points running mean both for altitude and temporal intervals, the data were processed further.

[10] The backscattering coefficients by particles (cloud and/or aerosol particles) at these two wavelengths,  $\beta_{532}$  and  $\beta_{1064}$ , were calculated from the observed lidar signal by using Fernald's algorithm [Fernald, 1984], assuming that the extinction to backscatter ratios (so-called lidar ratios) of cirrus clouds and aerosols are, respectively, 20 and 40 sr at 532 nm and 20 and 60 sr at 1064 nm, and that the lower stratospheric  $\beta_{532}$  at altitudes of about 20 km is 10% of the Rayleigh backscattering coefficient of atmospheric molecules.

[11] The lidar ratio could change with the size, shape and composition of the particles [e.g., Gobbi, 1995; Chen *et al.*, 2002; Sakai *et al.*, 2006]. The value 20 sr for cirrus cloud

was taken as the lidar ratio from cirrus at high altitudes observed by *Chen et al.* [2002]. This value is also within the Raman lidar observed values by *Sakai et al.* [2006] for the case of larger depolarization ratio. The value 40 sr of aerosols was calculated by the conditions of the volcanic aerosols by *Gobbi* [1995]. The values 40 and 60 sr at 532 nm and at 1064 nm, respectively, were also calculated by the authors using similar conditions to *Gobbi* [1995].

[12] The assumption for the calibration at 532 nm, or 10% of the Rayleigh backscattering coefficient of atmospheric molecules, is equivalent to assume backscattering ratio,

$$R_{\lambda} = \frac{\beta_{\lambda} + \beta_{m\lambda}}{\beta_{m\lambda}}, \quad (1)$$

equals 1.10, where  $\lambda$  is wavelength (here,  $\lambda = 532$  nm), and  $\beta_{m\lambda}$  is the backscattering coefficient at wavelength  $\lambda$  due to Rayleigh scattering of atmospheric molecules that was calculated using the data from the nearest balloon soundings in our analysis of the lidar data.

[13] For the calibration at 1064 nm it was also assumed that the color ratio (CR) (see below) of aerosols at the altitudes between 10 and 15 km and below cirrus clouds is 0.5, or the Angstrom exponent for backscattering of aerosols is 1.0. The Angstrom exponent  $\alpha$  of backscattering is the exponent if we assume  $\beta_{\lambda} \propto \lambda^{-\alpha}$ , where  $\lambda$  is wavelength. The values used for the calibration are calculated using the observed size distribution by OPC (see section 2.3 about the OPC) at each altitude in the campaign. The uncertainties of the derived values when using the assumed values in the lidar data analysis will be shown in section 4.3.

[14] The color ratio (CR) is defined by the ratio of the particle backscattering coefficient at 1064 nm to that at 532 nm, or

$$CR = \frac{\beta_{1064}}{\beta_{532}}. \quad (2)$$

The volume depolarization ratio (VDR) and particle depolarization ratio (PDR) are respectively defined as

$$VDR = \frac{\beta_{532\perp} + \beta_{m532\perp}}{\beta_{532//} + \beta_{m532//}} \quad (3)$$

and

$$PDR = \frac{\beta_{532\perp}}{\beta_{532//}}, \quad (4)$$

where  $\beta_{m532//}$ ,  $\beta_{m532\perp}$ ,  $\beta_{532//}$  and  $\beta_{532\perp}$  are, respectively, the parallel and perpendicular components of the backscattering coefficient of the molecules and particles with respect to the polarization plane of the linearly polarized laser beam at the wavelength of 532 nm. The VDR can be simply calculated as the ratio of the lidar signals at two polarization components. The PDR is, then, calculated from the VDR and  $R_{532}$  by the method shown in *Shibata and Yang* [2010]. In our analysis, we assumed that the particles are cirrus clouds (In other words lidar ratio is assumed to be 20) if the VDR is

larger than 0.1. This value of the VDR threshold was taken to be sufficiently larger than the values due to aerosol particles that are almost always smaller than a few percent in the upper troposphere over Biak.

[15] The lidar was operated from 6 to 13 January 2011 almost continuously (the observation was briefly interrupted several times by electrical power failures at the site, once for 3 h but otherwise only for a few minutes). There is also a gap in the data at 1064 nm from the evening on the 9th to the morning of the 11th due to a malfunction in the HV power supply of the APD detector.

### 2.3. Optical Particle Counter

[16] The OPC counts the number of pulses and measures the height of pulses scattered by aerosol particles in its scattering cell. The size of the particles is derived from the pulse height. A gear pump is used to introduce air into the scattering cell through its inlet tube at the flow rate of 3 L min<sup>-1</sup>. The OPC used a 780 nm laser diode as a light source and a silicon photo diode as a detector. The laterally scattered light from aerosol particles in the cell within a solid angle of 120 degrees is focused on the detector. The OPC counts the number of the particles larger than ten fixed threshold sizes. The threshold diameters ( $D_p$ ) are 0.3, 0.4, 0.5, 0.66, 0.8, 1.2, 2.0, 3.4, 7.0, and 11.4  $\mu\text{m}$  for the particles with a refractive index of 1.40–0i. The refractive index of the atmospheric aerosol particles may take values from 1.40 to 1.55 corresponding to the component of the aerosol particles. Some typical values are  $\sim 1.40$  (sulfuric acid solution), 1.53 (ammonium sulfate),  $\sim 1.50$  (sea salt), and  $\sim 1.55$  (mineral dust). The change in the values of refractive index from 1.40 to 1.59 will introduce a 10% and 20% error in the threshold diameter, respectively, at submicron size and at micron size particles. Although uncertainty by a factor of 2 in number concentration at the fixed threshold sizes shown above could be caused by this error, it will not affect the conclusions of this paper.

[17] The OPC is lightweight (1.1 kg) and compact in size (22 cm wide, 18 cm deep, 19 cm high), and it can be launched on a small rubber balloon. It was launched with Meisei RS06G radiosonde that transmitted the observed data every 4 s. Since the ascending speed of the balloon is set at 5 m s<sup>-1</sup>, the vertical resolution of the data is 20 m. We finally integrated data for each 200 m (40 s) to improve the statistics of the data. Therefore, for this resolution the volume of the air sampled by OPC is 2 L according to the flow rate (3 L min<sup>-1</sup>) of the gear pump. The detection limit of the OPC is determined as 1 count per 40 s interval, or 0.5 particle L<sup>-1</sup>.

[18] In the work reported here we also used an OPC with an inlet tube that was heated to 200°C. The weight of the heated inlet tube is 2.8 kg. This temperature is higher than the boiling point of sulfuric acid aqueous solution aerosol particles [*Rosen*, 1971]. Although the temperature is also higher than the temperature at which solid sulfate compositions (ammonium sulfate etc.) evaporate [*Huffman et al.*, 2008], our laboratory experiments using our OPC system showed that more than 90% of the solid sulfate particles were also counted after heating to 200°C. This is probably because, in our OPC system, the time to pass through the heater before the particle-count is shorter than the time for full evaporation. The complete evaporation of sulfuric acid

particles was confirmed by the laboratory experiments at 200°C heated condition. Therefore, the profiles obtained by using the 200°C heated inlet give the profile of both volatile and non-volatile solid particles at 200°C such as sulfate and sea salt, mineral dust, and volcanic ash. We launched a single ordinary OPC without a heated inlet tube on the 7th (results are not shown here), and launched two OPCs (an ordinary OPC and an OPC with a heated inlet tube) simultaneously in the afternoon on the 10th. The volatility of aerosol particles was measured by the two OPCs during this simultaneous flight. The observed results from the OPCs were compared with the results from the lidar. Details of the OPC are found in *Hayashi et al.* [1998], *Hayashi* [2001], and *Iwasaki et al.* [2007].

#### 2.4. Cryogenic Frost Point Hygrometer

[19] The cryogenic frost point hygrometer (CFH) was utilized to observe water vapor profiles. The CFH was launched with an electrochemical concentration cell (ECC) ozonesonde and a VAISALA RS80 radiosonde. The CFH measured the frost point temperature. The water vapor pressure was calculated as the saturation vapor pressure at the frost point temperature using the Goff-Gratch equation. The same equation is used to calculate the saturation vapor pressure at the ambient temperature. The concentration or the mixing ratio of water vapor, and relative humidity are calculated using these vapor pressures. The measurement uncertainty in the CFH was estimated to be between less than 4% in the tropical troposphere to no more than 10% at 28 km in altitude by *Vömel et al.* [2007]. The CFH is designed to measure water vapor concentrations accurately from the ground to the middle stratosphere including the very dry regions around the tropical tropopause. Details of the CFH are found in *Vömel et al.* [2007].

### 3. Results

[20] Figure 1 shows the lidar-observed backscattering coefficient at 532 nm from 6 to 13 January 2011. An optically thin aerosol layer between 17.5 and 19 km in altitude was continuously observed throughout this period just above the CPT at about 18 km in altitude (see Figure 3a). Since no layer at the same altitude was visible in VDR or PDR (See Figure 4b), both VDR and PDR were no more than a few percent. The  $\beta_{532}$  of the layer was smaller than  $1.0 \times 10^{-7} \text{ msr}^{-1}$ , which is much smaller than for the cirrus clouds observed at altitudes below the CPT. The yellow to red colored regions ( $1.0 \times 10^{-6}$ – $1.0 \times 10^{-5} \text{ msr}^{-1}$ ) at around 14 to 17 km in altitude are due to the stronger backscattering from cirrus clouds. The profiles of the aerosol layer were more stable than the profiles of the cirrus clouds and did not show diurnal (or shorter) variation like that shown by the cirrus clouds. The height of the bottom of the cirrus clouds showed clear diurnal variation, being lowest in the late afternoon and early morning from the 6th to the 11th. Similar diurnal variation was reported in *Fujiwara et al.* [2009]. There were two sub-layers in the aerosol profiles of Figures 1a–1c. The bottom of the lower aerosol layer was in contact with the top of the cirrus cloud between 17:00 to 23:00 LT on the 8th (Figure 1c). There were three cases in which cirrus cloud appeared at about 17.5 km in the aerosol layer: between 13:00 and 16:00 LT on the 11th, between 03:00 and 06:00 LT on the 12th (Figure 1f), and between 00:00 and 04:00 LT on

the 13th (Figure 1g). In the second case, the cirrus appearance was in the center of the aerosol layer.

[21] Figure 2 shows the OPC observed profiles of aerosol particles larger than each threshold diameter shown by the legend in Figure 2b. Figures 2a and 2b respectively show the profiles observed without and with a heated inlet. The two OPCs were launched simultaneously on the same balloon at 11:30 LT on the 10th, and reached an altitude of 20 km at 12:27 LT. The corresponding lidar profile is shown in Figure 1e, in which the time-altitude trajectory of these OPCs is shown as a broken white line. Unfortunately, the lidar profiles were available only soon after the OPC observations, since there were dense clouds at low altitude for the period of the balloon flight of the OPCs. The aerosol layer is also clearly seen in the profiles of the particles larger than 0.3 and 0.4  $\mu\text{m}$  observed at the ambient temperature with an unheated inlet (Figure 2a). We can see a low maximum at the same height of the layer in the profile of the smallest size by the OPC with a heated inlet (Figure 2b), but the concentration of those particles is a few percent of the concentration measured by the OPC without the heated inlet (at the ambient temperature).

[22] Figure 2c shows the ratio of the particle number due to heated inlet compared to the number due to ambient conditions. The ratio of smaller size (solid line,  $D_p > 0.3 \mu\text{m}$ ) took minimum value in the upper half of the aerosol layer, and small maximum in the lower half. The ratio of larger size (broken line,  $D_p > 0.8 \mu\text{m}$ ) shows similar variation for altitude. Figure 2d shows the  $\beta_{532}$  observed by lidar soon after the OPC observations. The peak at 16.6 km in altitude is a cirrus cloud. The altitude of this cirrus cloud is within the broad maximum of the ratio in larger size from 16 to 17 km in altitude shown in Figure 2c.

[23] Figure 3a shows the CFH observed vertical profile of frost point temperature ( $T_p$ ), ambient temperature ( $T$ ) and threshold temperature ( $T_{\text{NAT}}$ ) of nitric acid tri-hydrate (NAT).  $T_{\text{NAT}}$  was obtained using the results of *Hanson and Mauersberger* [1988], and by assuming 1 ppbv of  $\text{HNO}_3$  and using the ambient water vapor pressure observed by CFH. Figures 3b, 3c, and 3d respectively depict the mixing ratio and saturation-mixing ratio of  $\text{H}_2\text{O}$ , relative humidity over ice obtained from the  $T_p$  and  $T$  in Figure 3a, and nearest lidar profile averaged between 17:50 and 17:55 LT. The CFH was launched at 17:07 LT on the 10th and reached an altitude of 20 km at 18:00 LT. The corresponding lidar profile is also shown in Figure 1e, in which the time-altitude trajectory of the CFH is shown as a broken purple line. The Rhi was about 80% at 17.7 km (in the lower half of the aerosol layer) and decreased to less than 20% at altitudes higher than 18.2 km (in the upper half of the aerosol layer). Within the aerosol layer the humidity changes drastically: from very humid in the lower half to very dry in the upper half. The Rhi took a highly supersaturated maximum value (130%) where a cirrus cloud was observed at 16.8 km (Figure 1e and Figure 3d). High supersaturation over ice within cirrus clouds like this had often been observed in previous SOWER campaigns [*Shibata et al.*, 2007]. The mixing ratio in Figure 3b is increasing or constant at this height of Rhi decrease. Therefore, the Rhi decrease at the altitude of 18 km was caused by ambient temperature increase above this height due to entering the stratosphere. Since  $T$  is lower than  $T_{\text{NAT}}$ , NAT

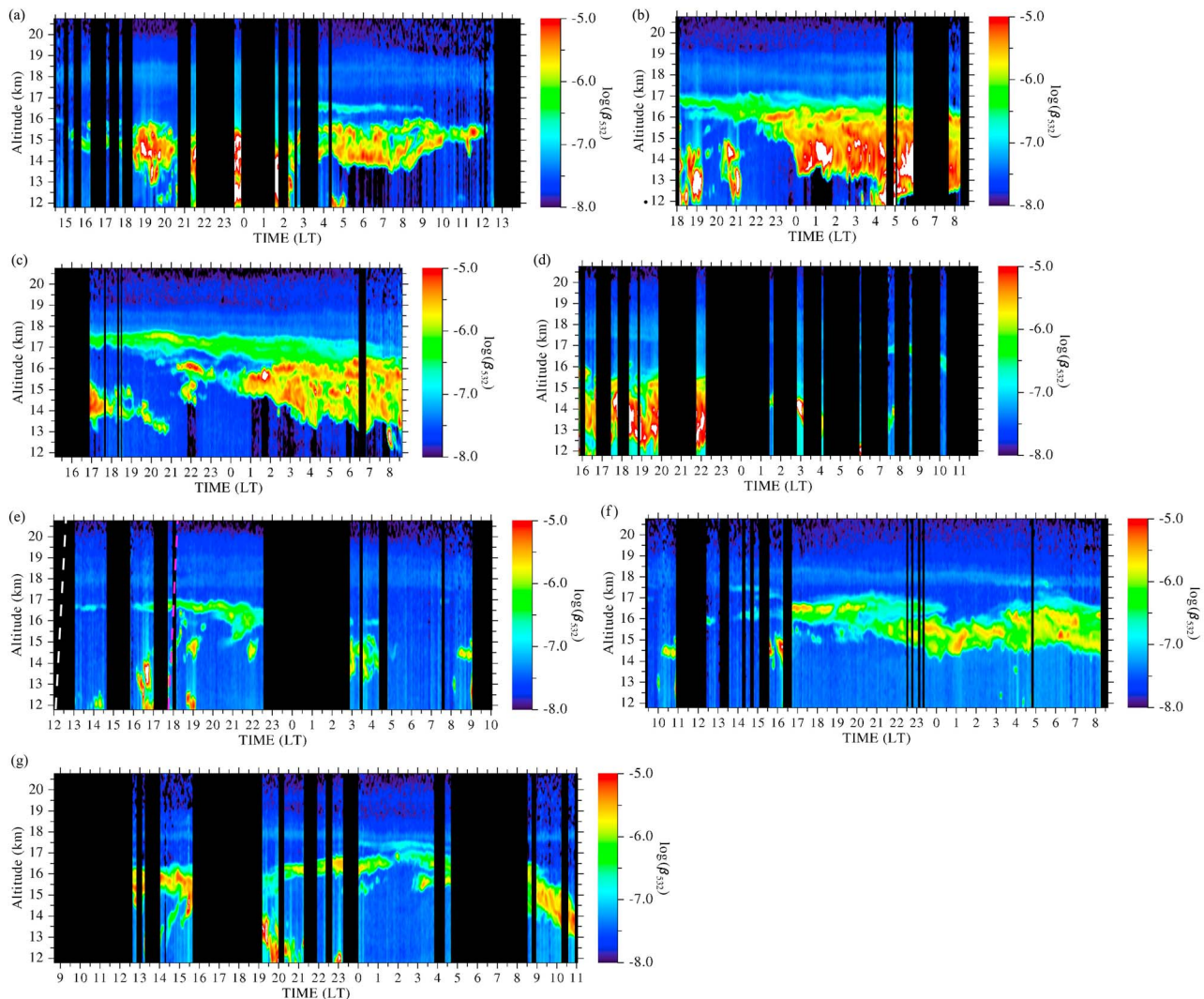


**Figure 1.** The backscattering coefficient at 532 nm,  $\beta_{532}$  ( $\text{msr}^{-1}$ ), observed by lidar from 6 to 13 January 2011: (a) 6 to 7 January, (b) 7 to 8 January, (c) 8 to 9 January, (d) 9 to 10 January, (e) 10 to 11 January, (f) 11 to 12 January, and (g) 12 to 13 January. An aerosol layer at about 18 km (above the very variable cirrus cloud layer) was observed almost continuously throughout the survey. Periods with low-quality data are masked by black bars. The white and purple broken lines in Figure 1e are respectively approximate time-altitude trajectories of optical particle counters (OPCs) and a cryogenic frost-point hygrometer (CFH) whose data are shown in Figure 2 and Figure 3.

can be stable in the TTL region from 15.5 to 18 km in altitude as shown in Figure 3a.

#### 4. Discussion

[24] In this section we will discuss the aerosol layer just above CPT observed continuously through the survey period, the cirrus clouds that appeared in it, and the uncertainty of the values derived from the lidar data.

##### 4.1. Aerosol Layer

[25] The lidar observed properties of the aerosol layer just above the CPT are very different from the properties of cirrus clouds. The PDR and CR of the layer were lower than 0.05 and 0.5, respectively (see Figure 4, between 01:00 and 02:00 LT at an altitude of about 18.2 km), whereas the

typical PDR and CR values for cirrus clouds are  $\sim 0.4$  (PDR) and  $\sim 1.0$  (CR) [Shibata *et al.*, 2007; Vaughan *et al.*, 2010]. Furthermore, the vertical profile of the layer was much more stable than the lower cirrus clouds at altitudes 14 to 17 km. Although the altitude, width and density ( $\beta_{532}$ ) of the cirrus clouds changed within at most a half-day, the altitude, width and density of the layer were almost constant throughout the week during which they were measured. The aerosol layer was between 17 and 19 km at least for one week of the survey period. In the afternoon of the 10th, the upper half of the layer was very dry ( $\text{Rhi} < 20\%$ ), but the lower half was very humid ( $\text{Rhi} \approx 80\%$ ). Therefore, the layer was situated on the boundary of the humid troposphere and dry stratosphere.

[26] Several compositions are possible for this enhanced aerosol layer: type I PSC like particles composed of NAT or

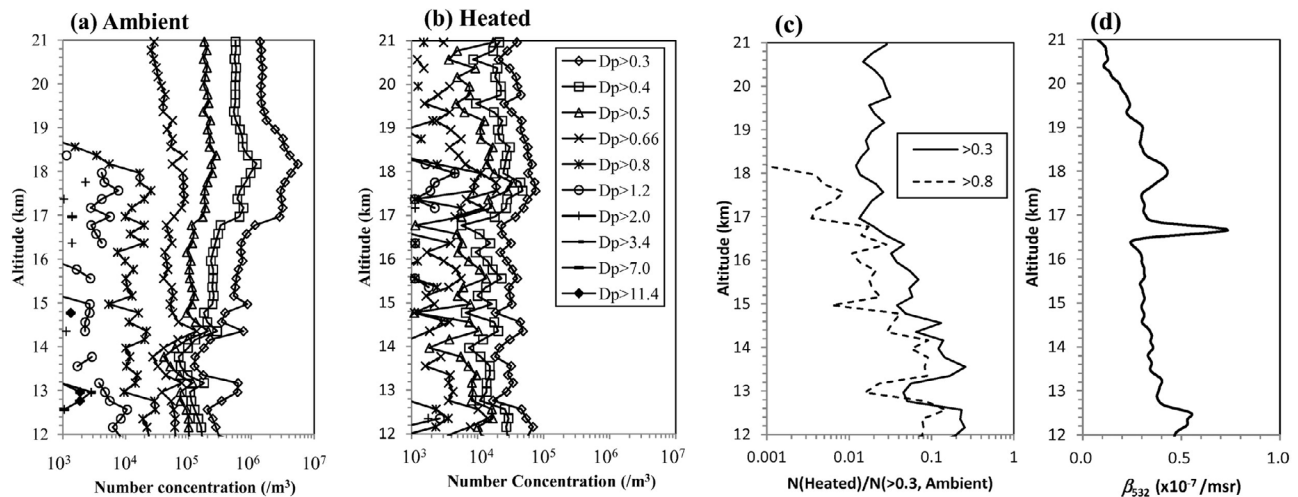


**Figure 2.** (a) Profiles of the concentration of aerosol particles larger than each threshold diameter ( $D_p$ , in  $\mu\text{m}$ ) shown in the legend that were counted by an OPC without a heated inlet tube (observed at ambient temperature). (b) Profiles of the concentration of aerosol particles larger than each threshold diameter ( $D_p$ , in  $\mu\text{m}$ ) shown in the legend that were counted by an OPC with a heated inlet tube (at  $200^\circ\text{C}$ ). OPCs were launched on the same balloon at 11:30 LT on 10 January and reached an altitude of 20 km at 12:21 LT. The inset key in Figure 2b is for both Figures 2a and 2b. (c) Profiles of the ratio of heated to ambient concentrations observed by OPCs. Broken line indicates the ratio  $N(D_p > 0.8 \mu\text{m}, \text{heated})/N(D_p > 0.3 \mu\text{m}, \text{ambient})$ . Solid line indicates the ratio  $N(D_p > 0.3 \mu\text{m}, \text{heated})/N(D_p > 0.3 \mu\text{m}, \text{ambient})$ . (d) Lidar observed  $\beta_{532}$  averaged from 13:35 to 14:00 LT on 10 January. Horizontal scale is linear.

super cooled ternary solutions (STS), sulfuric acid water droplets originating from volcanic eruption, and thin cirrus clouds. The possibility of cirrus clouds is excluded by the low PDR of the layer (Figure 4b) and the very dry condition in the upper half of the layer (Figure 3c). The possibilities of NAT and STS are also excluded by the relation of  $T > T_{\text{NAT}}$  in the same upper half of the layer (Figure 3a), and by the

relation of  $T_{\text{NAT}} > T_{\text{STS}}$  from the conditions at this altitude [Hanson and Mauersberger, 1988; Tabazadeh et al., 1994; Carslaw et al., 1995; Shibata et al., 1999]. According to these temperature limitations particles composed of NAT or STS cannot be stable at an altitude higher than about 18 km. Therefore, in the compositions listed above, only the sulfuric

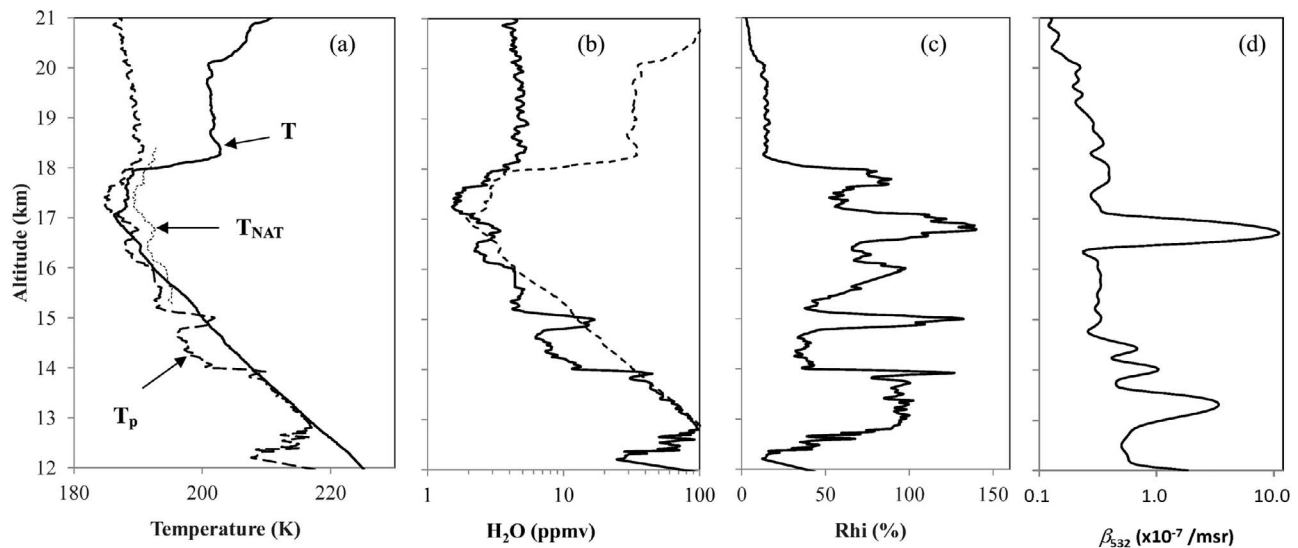


**Figure 3.** (a) Profiles of atmospheric temperature ( $T$ ), frost point temperature ( $T_p$ ) and critical temperature of NAT ( $T_{\text{NAT}}$ ). (b) CFH observed water vapor mixing ratio (solid line) and water vapor saturation mixing ratio (broken line). (c) CFH observed relative humidity over ice. The balloon was launched at 17:07 LT on 10 January 2011 and reached an altitude of 20 km at 18:00. (d) Lidar observed  $\beta_{532}$  averaged from 17:50 to 17:55 LT on 10 January. Horizontal scale is logarithmic.

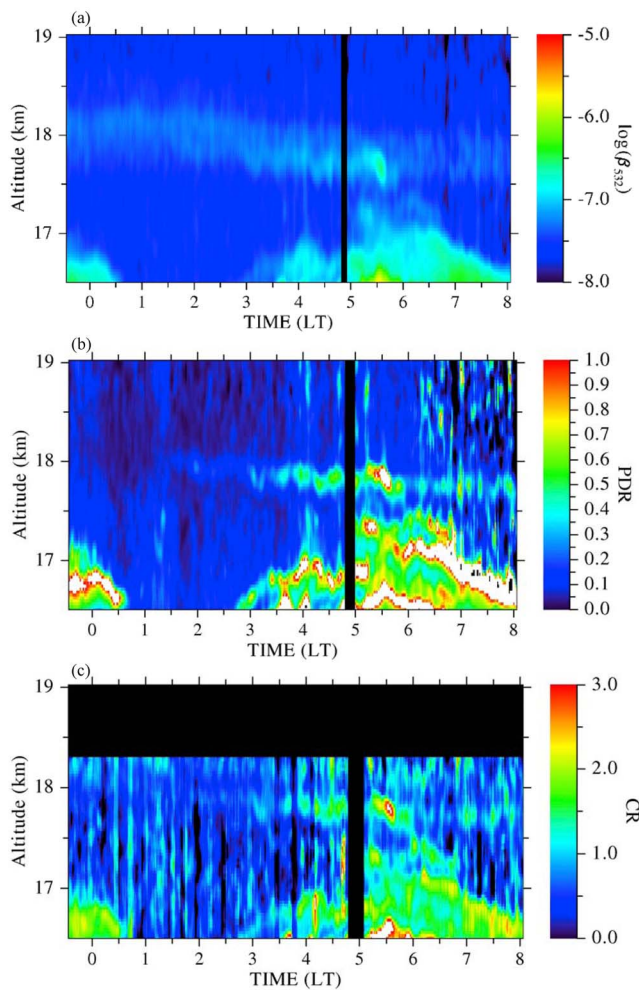


**Figure 4.** (a) Time-altitude plot of  $\beta_{532}$  ( $\text{msr}^{-1}$ ) for the expanded time-altitude region on 12 January in Figure 1f. (b) Time-altitude plot of particle depolarization ratio (PDR) at the wavelength of 532 nm for the same time-altitude region as in Figure 4a. The depolarization by the aerosol layer was very small or not detectable. At 03:00 to 06:00 LT, enhanced depolarization was seen at the altitudes between 17.5 and 18 km. The depolarization at these altitudes is as large as 0.5. (c) Time-height plot of CR on 12 January. The cirrus cloud layer shows a CR similar to that of the lower cirrus clouds. The color ratio (CR) in the aerosol layer is smaller than 1, a value typical for aerosols. Areas with noisy data are masked. (Since there are many time-height regions in Figure 4b where PDR is larger than 1.0, the absolute value of PDR could be over estimated.)

acid water droplets originating from volcanic eruption are possible composition of the enhanced aerosol layer.

[27] As was shown in section 3, the OPCs observed that the particles of the aerosol layer are in the submicron size and most of the particles were evaporated at 200°C. The small depolarization suggests that the particles are in the liquid phase. These observed characteristics suggest that the aerosol layer was composed of sulfuric acid aerosol droplets and was probably of volcanic origin.

[28] Hayashi [2001] observed newly formed aerosol layer in the Aitken mode ( $<0.1 \mu\text{m}$ ) at the altitude of the CPT over Bandung, Indonesia on 26 September 2000 by using another type of OPC. They suggested that the number of particles in the Aitken mode was increased by a particle formation under the low temperature condition of the tropical tropopause. Although the aerosol layer observed in January 2011 could be formed by the same mechanism at similar low temperature conditions, some additional material is needed so that the newly formed particles are able to grow larger than the sizes in the background condition, supporting the suggestion that the layer was a volcanic aerosol layer.

[29] It was reported that the Indonesian volcano Merapi in the center of Java island ( $7.5^\circ\text{S}$ ,  $110.4^\circ\text{E}$ ) erupted from the end of October to the beginning of November 2010 (Smithsonian National Museum of Natural History, Global Volcanism Program; <http://www.volcano.si.edu/>). The ash plume from an eruption on 3 November rose to an altitude of 18.3 km. Since there is no report of another large volcanic eruption at low latitudes at the end of 2010, the eruption of Merapi is the most likely source of the lidar observed aerosol layer.

[30] Volcanic clouds originating from relatively small eruptions are often detected by space-borne lidar CALIOP (Cloud-Aerosol Lidar with Orthogonal Polarization) on board the satellite CALIPSO (Cloud-Aerosol Lidar Infrared Pathfinder Satellite Observations) [e.g., Shibata and Kouketsu, 2008]. The lidar observed aerosol layer at Biak cannot be seen in January 2011 in the browsing images of CALIOP observation ([http://www-calipso.larc.nasa.gov/products/lidar/browse\\_images/](http://www-calipso.larc.nasa.gov/products/lidar/browse_images/)), but is visible in November 2010 in the images at the same level of the layer observed by Biak lidar. Although detailed analysis is needed if the satellite borne lidar data is to be used to determine the horizontal distribution of the aerosol layer [e.g., Vernier et al. 2009], the CALIOP data probably supports the Merapi eruption as being the source of the layer.

#### 4.2. Cirrus Cloud Appearing in the Aerosol Layer

[31] As written above, an aerosol layer was observed at around 18 km, just above the cirrus clouds. On the other hand, there was a case in which a cirrus cloud appeared in the center of the aerosol layer between 03:00 and 06:00 LT on the 12th and at an altitude between 17.5 and 18 km (Figure 1f). Figure 4 shows the plots of  $\beta_{532}$ , PDR, and CR for the expanded time altitude region.

[32] On 12 January 2011 the PDR at 18 km began to increase at around 2:00 A.M., and reached its maximum value at 5:30 A.M. (Figure 4b). The time-altitude region of the increase in PDR was the same as the time-altitude region of increase in  $\beta_{532}$  (Figure 4a). An increase in CR was also observed in the same time-altitude region (Figure 4c). The CR values of the layer outside of the time-altitude region in which CR increased were less than 1. This smaller CR region corresponds to the aerosol, and the smaller CR is consistent with the CR due to an aerosol (see below).

[33] In the case above, it apparently seems that the cirrus cloud was formed in situ within the aerosol layer. It is, however, possible that the cirrus cloud was formed by a deep convection that arrived at the altitude of the cloud. As described in section 3, the OPC observed that the

concentration of the coarse mode particles ( $0.8$  and  $1.2 \mu\text{m}$ ) was higher in the lower half of the layer. The vertical distribution of coarse mode particles suggests that at least the lower atmosphere may affect the lower half of the aerosol layer, probably by deep convection. We have checked the equivalent blackbody temperature ( $T_{\text{bb}}$ ) at the infrared window channel IR1 ( $10.3\text{--}11.3 \mu\text{m}$ ) observed by a weather satellite MTSAT2 to ascertain whether such a deep

convection occurred near Biak. For more than one week windward of Biak at the altitude of the cirrus cloud, and from 4 to 11 January 2011, there was small area of deep convection for which the  $T_{\text{bb}}$  was very low ( $<200$  K). Figure 5a shows one-week backward trajectories calculated by using ECMWF operational analysis data starting from 81 points within a circle centered at Biak with the radius of  $0.5$  degree at  $17.8$  km in altitude and from 5:00 (LT) on 12 January. Figures 5b, 5c, and 5d show temperature history (blue lines, most of the lines overlap) calculated by the trajectories and  $T_{\text{bb}}$  (light blue dots) under the trajectories started at 05:00 LT, 04:00 LT and 03:00 LT, respectively. The  $T_{\text{bb}}$  under the trajectories is higher than  $210$  K in all the cases of the backward trajectory started at 05:00 LT. The  $T_{\text{bb}}$  under a few trajectories started at 04:00 LT (Figure 5c) and 03:00 LT (Figure 5d) show temperatures as low as  $200$  K at around 08:00 UT ( $17:00$  LT) on the 11th. This lower temperature was caused by the trajectories passing near a low  $T_{\text{bb}}$  region of a small-scale tropical convection on the northern coast of Papua New Guinea. The equivalent blackbody temperature  $T_{\text{bb}}$  is more than  $15$  K higher than the ambient temperature  $T$ . Hamada and Nishi [2010] estimated cloud top height by comparing  $T_{\text{bb}}$  at  $10.8 \mu\text{m}$  (IR1) and  $12 \mu\text{m}$  (IR2) with the data by CloudSat from July 2006 to June 2008. The estimated cloud top height at  $200$  K and  $210$  K of  $T_{\text{bb}}$  at IR1 are not higher than  $17$  and  $16$  km in altitude, respectively. Furthermore, the difference of  $T_{\text{bb}}$  (IR3,  $6.5\text{--}7.0 \mu\text{m}$ ) in the water vapor absorption band and  $T_{\text{bb}}$  (IR1) in all the areas including the trajectory does not show a positive value at the time when  $T_{\text{bb}}$  was lowest under the trajectories on 11 January. The difference,  $T_{\text{bb}}(\text{IR3}) - T_{\text{bb}}(\text{IR1})$ , will show positive value if the top of convection is in TTL [Schmetz et al., 1997; Iwasaki et al., 2010]. Therefore, it seems unlikely that the cirrus cloud was formed in a deep convection, injected into the observed altitude, and transported to the observation site. The cirrus cloud was probably formed in situ as is seen in the observed profile.

[34] The temperature histories (Figures 5b–5d) (blue lines) show that the temperature of the air parcel including the thin cirrus clouds was constant or slightly increasing before arriving at Biak. This temperature change may suggest that the accuracy of the temperature as obtained from ECMWF would not be enough especially to estimate the temperature near CPT

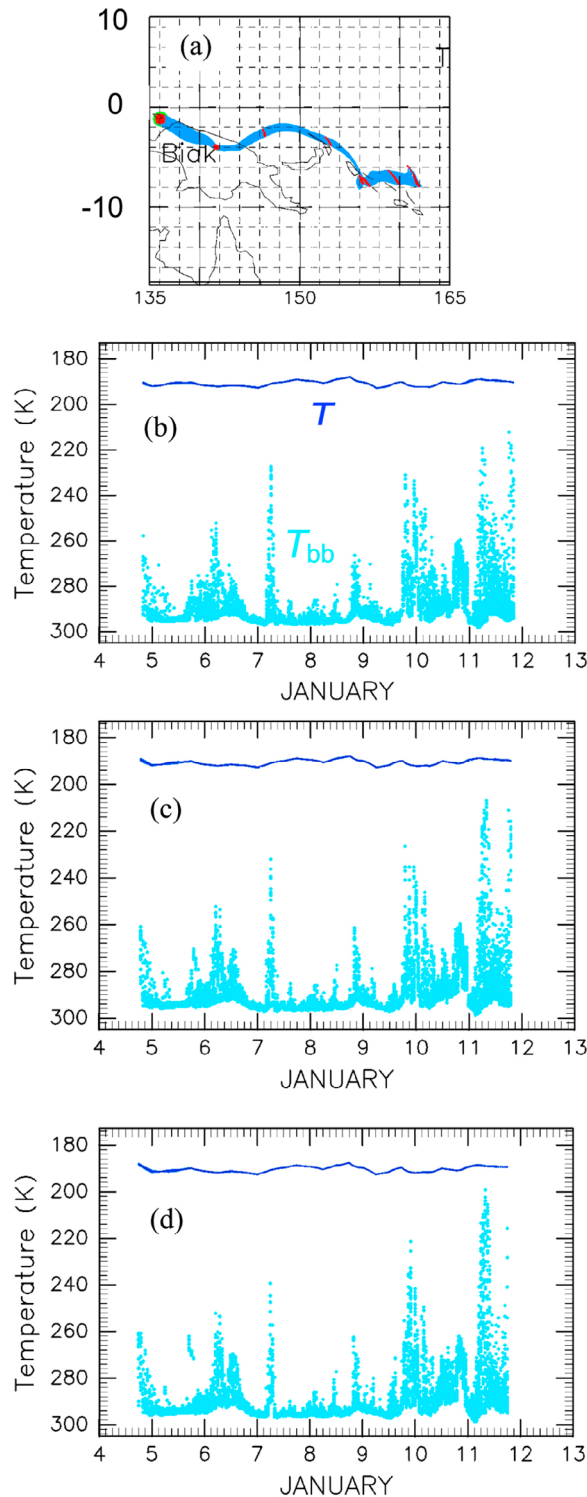


**Figure 5.** (a) Backward trajectories (blue lines) calculated by using the European Center for Medium Range Weather Forecasts (ECMWF) operational analysis data. The color is changed to red for each 24 h. (Here the 81 lines contact and look like a bold line.) The initial points of trajectories are at 20:00 UT 11 January 2011 (05:00 LT 12 January 2011),  $17.8$  km in altitude and at 81 points within a circle whose radius is  $0.5$  degree with the separation of  $0.1$  degree. (b) Ambient temperature of the air parcel (blue lines) and  $T_{\text{bb}}$  under the air parcel (light blue points) for 7 days of the backward trajectories in Figure 5a. (c) Same as Figure 5b but the backward trajectories started at 19:00 UT 11 January (04:00 LT 12 January). (d) Same as Figure 5b but the backward trajectories started at 18:00 UT 11 January (03:00 LT 12 January). The abscissa of F Figures 5b and 5c is in UT (= LT - 9 h).

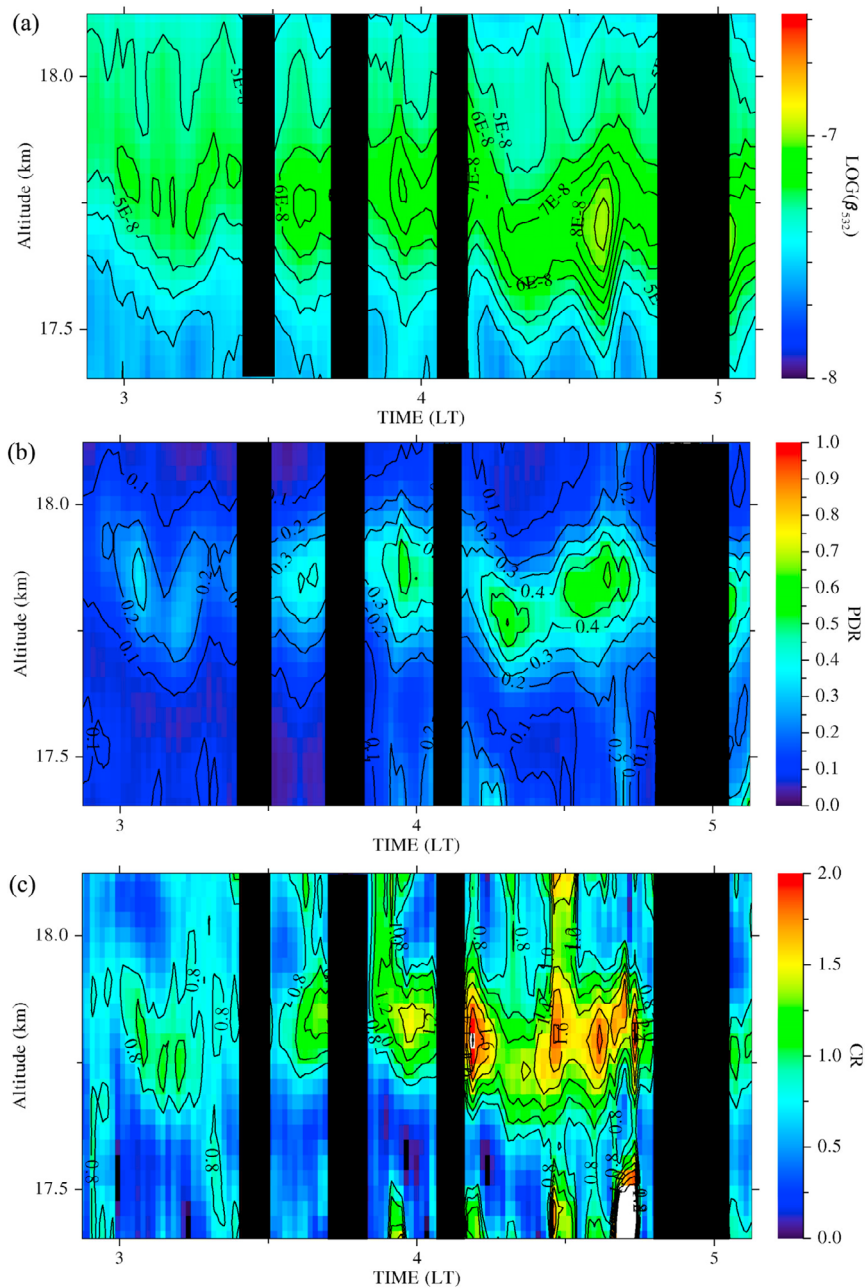


**Figure 6.** Same as Figure 4 for the expanded area from 02:50 to 05:10 LT and from 17.4 to 18.1 km in altitude.

where there is a fine vertical structure of temperature, or that smaller scale dynamics like gravity wave decreased temperature to form cirrus clouds [Jensen *et al.*, 2010].

[35] The scattering properties of the enhanced backscattering layer shown in Figure 4 observed at about 18 km from 2:00 to 8:00 A.M. on 12 January 2011 correspond to microphysical properties of cirrus clouds. In order to look at this enhanced layer closely, Figure 6 depicts the further expanded Figure 4 for the region between 02:50 to 05:10 LT and 17.4 to 18.1 km in altitude. By using  $\beta_{532}$  and CR, the number concentration of cirrus cloud particles can be

estimated by scattering theory if we can assume the particles are spherical. Here we assumed a lognormal size distribution for the ice particles:

$$\frac{dn}{dr} = \frac{N}{\sqrt{2\pi r \ln \sigma}} \exp\left(-\frac{(\ln r - \ln r_g)^2}{2 \ln^2 \sigma}\right) \quad (5)$$

where  $n$  is the size distribution function,  $r$  is the particle radius,  $N$  is total ice particle number concentration,  $r_g$  is the mode radius, and  $\sigma$  is the standard deviation. Ice particles are assumed to be homogeneous spherical shaped for Mie

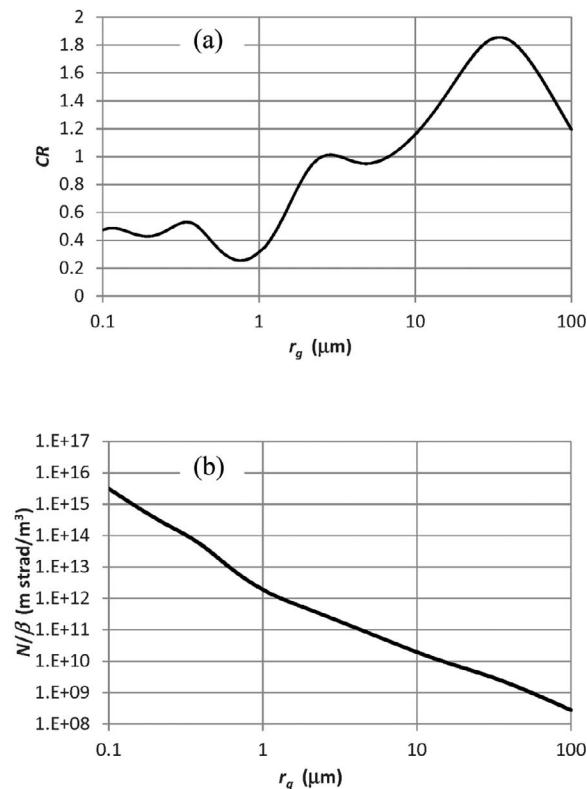


**Figure 7.** Relation between (a) mode radius  $r_g$  in equation (5) versus CR, and (b)  $r_g$  versus  $N/\beta_{532}$  calculated using Mie scattering theory.

scattering theory. Figure 7 shows the calculated relation between  $r_g$  and CR (Figure 7a), and  $r_g$  and  $N/\beta_{532}$  (Figure 7b). We assumed  $\sigma = 1.5$  and calculated these relations for the size distribution by changing the parameter  $r_g$  from  $0.1 \mu\text{m}$  to  $100 \mu\text{m}$ . The interval of the integration is  $0.01$  to  $300 \mu\text{m}$ . The refractive index of ice for each wavelength of the laser is taken from Warren [1984]. As can be seen in Figure 7a, relation between  $r_g$  and CR is almost one-to-one if the mode radius of the particles is from  $2$  to  $30 \mu\text{m}$ , although there is an exception in that  $r_g$  can be  $4$  to  $7 \mu\text{m}$  if CR is near around  $1.0$ . Since previous studies indicate that the radius of the TTL cirrus is about several micrometers [e.g., Peter et al., 2003; Shibata et al., 2007; Lawson et al., 2008; Jensen et al., 2010], we assumed that the size of the cirrus cloud is in this one-to-one relation. For this range,  $N/\beta_{532}$  has values between  $10^{10}$  and  $10^{12} \text{sr m}^{-2}$ . At around from 03:00 to 03:30 LT, CR is about  $0.8$ , and  $\beta_{532}$  is  $5 \times 10^{-8} \text{msr}^{-1}$  at  $17.8 \text{ km}$  in altitude. The mode radius  $r_g$  correspond to CR =  $0.8$  is  $2 \mu\text{m}$ , and  $N/\beta_{532}$  is  $5 \times 10^{11} \text{sr m}^{-2}$  by Figures 7a and 7b. This  $\beta_{532}$  gives  $N = 2.5 \times 10^4 \text{m}^{-3}$ . Since CR is  $\sim 1.4$  and  $\beta_{532}$  is  $7 \times 10^{-8} \text{msr}^{-1}$  at  $17.8 \text{ km}$  in altitude at 04:00 LT and 04:30 LT, the estimated number is  $\sim 7 \times 10^2 \text{m}^{-3}$  at these times.

[36] As will be shown in section 4.3, the estimated relative error of CR is about  $\pm 30\%$ . For the case of CR =  $0.8$ , the uncertainty of CR is  $0.8 \pm 0.24$ . The uncertainty in  $N/\beta_{532}$  caused by this amount of uncertainty in CR, ranges over nearly three orders of magnitude from  $3 \times 10^{10}$  to  $1 \times 10^{12} \text{sr m}^{-2}$ . The uncertainty of the estimated N ranges from  $1.5 \times 10^3$  to  $5 \times 10^4 \text{m}^{-3}$ . In the same way, for the case of

CR =  $1.4$ ,  $N/\beta_{532}$  ranges from  $4 \times 10^9$  to  $4 \times 10^{11} \text{sr m}^{-2}$ , and the uncertainty of the estimated N ranges from  $2.8 \times 10^2$  to  $2.8 \times 10^4 \text{m}^{-3}$ . Therefore, for the estimation of number by using the relations in Figure 7, the values of N obtained by our lidar observations may have an uncertainty of about two orders of magnitude. These estimated number concentrations are from one to two orders of magnitude smaller than  $10^5 \text{m}^{-3}$  from the previous studies [e.g., Jensen et al., 2010] even when considering the uncertainty in our lidar observations.

[37] In the estimation above, we assumed a spherical shape for the cirrus cloud particles. For the TTL cirrus, this assumption may be partly supported by the observation by Lawson et al. [2008]. They observed that the ice particles in TTL are nearly spherical shaped if they are smaller than  $65 \mu\text{m}$ . However, lidar observed large depolarization of the thin cirrus clouds, as shown in Figures 4 and 6, indicates that the cirrus cloud particles cannot be treated as perfect spheres by Mie scattering theory.

[38] Figure 8 depicts the scattering properties of randomly oriented spheroid particles calculated by using T-matrix method [Mishchenko and Travis, 1998]. Spheroid particles are formed by rotating an ellipse about its minor (oblate spheroid) or major (prolate spheroid) axis. Each plot in Figure 8 shows the calculated PDR (Figure 8a), CR (Figure 8b), and  $N/\beta_{532}$  (Figure 8c). Colors (or contour lines) show the values of these parameters. The ordinate shows the aspect ratio (AR) of the particles, or the ratio of the horizontal to rotational axes. The ratio AR =  $1$  means the shape is a perfect sphere, AR >  $1$  oblate spheroid, and AR <  $1$  prolate spheroid. The abscissa shows  $r_g$  as defined by equation (5). The size of the spheroid particles is specified in terms of the equal-volume sphere radius. The calculated CR for the sphere particles by Mie scattering and by T-matrix method coincide within the difference of  $0.1\%$ . Since the integration interval for calculating the values in Figure 8 for the lognormal size distribution (equation (5)) is  $0.1$  to  $10 \mu\text{m}$ , the results near the boundary of the abscissa (smaller than  $\sim 0.5 \mu\text{m}$  and larger than  $\sim 8 \mu\text{m}$ ) are affected by this truncation of the integration interval (neither the smaller or larger side of the size distribution, respectively, are included in the integration). The calculated range of AR is  $1 \pm 0.1$ , and the shape is slightly non-spherical particles. PDR takes larger values than  $0.3$  if AR is larger than  $1.02$  or smaller than  $0.98$  (Figure 8a), or particles show large depolarization like cirrus cloud (PDR >  $30\%$ ) for only  $2\%$  deformed sphere.

[39] CR (Figure 8b) monotonically increases from  $0.4$  to  $1.0$  with  $r_g$  without depending on AR when  $r_g$  is between  $1$  and  $2 \mu\text{m}$ . For the larger particles the relation between CR and  $r_g$  is complicated and is highly dependent on AR. The relation between CR and  $r_g$  is not one-to-one. CR is larger than  $1.2$  when  $r_g$  is at  $10 \mu\text{m}$  for sphere (Figure 7a), but is larger than  $1.2$  at about  $2 \mu\text{m}$  for a spheroid if AR is smaller than  $0.95$  or larger than  $1.07$ . These results indicate that the estimation of  $r_g$  from CR is not possible if we consider the nonsphericity of the cirrus cloud particles and if CR is larger than  $\sim 1.0$ .

[40] Although we can't determine  $r_g$  by the given CR if there is no information on shape (AR) of the particles, it is probably possible to estimate the upper limit of  $N/\beta_{532}$  even in such cases. For the particles whose  $r_g$  is larger than  $1.5 \mu\text{m}$ ,  $N/\beta_{532}$  (Figure 8c) is smaller than  $1 \times 10^{12} \text{sr m}^{-2}$ . Since the estimated size of TTL cirrus cloud particles according to

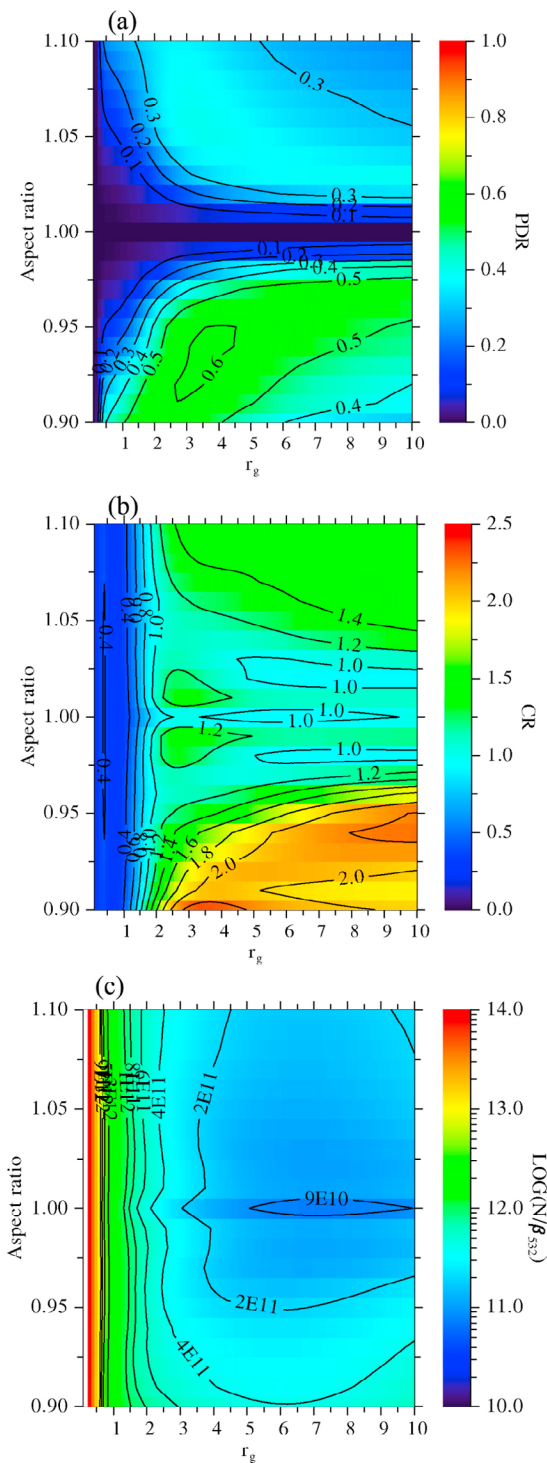


**Figure 8.** Relation between (a) mode radius  $r_g$  and (AR) versus PDR, (b) mode radius  $r_g$  and AR versus CR, and (c) mode radius  $r_g$  and aspect ratio (AR) versus  $N/\beta_{532}$  calculated by  $T$ -matrix method.

previous studies is several micrometers as written above, if we assume the mode radius of the cirrus cloud particles to be between 2 and 10  $\mu\text{m}$ , the upper limit of  $N$  can be calculated by using this value of  $N/\beta_{532}$  ( $1 \times 10^{12} \text{ sr m}^{-2}$ ) and  $\beta_{532}$ .

[41] The CR of the cirrus cloud was more than 2 at about 05:30 LT (Figure 4c). These values are larger than the value estimated by assuming homogeneous spherical ice particles. This may be partly because of the greater noise in CR and/or the nonspherical shape of the grown ice particles (Figure 8b). Lawson *et al.* [2008] also observed that the ice particles are highly nonspherical if particles are larger than 65  $\mu\text{m}$ . With a larger  $\beta_{532}$  there would be more enlarged particles at the specified altitude and time.

[42] The observed CR and  $\beta_{532}$  of the cirrus cloud of Figure 6 in the period from 03:00 to 05:00 LT took values between 0.8 and 1.7 and between  $5 \times 10^{-8}$  and  $1 \times 10^{-7} \text{ msr}^{-1}$ , respectively. Using the  $N/\beta_{532} = 1 \times 10^{12} \text{ sr m}^{-2}$ , the upper limit of  $N$  is estimated from  $5 \times 10^4$  to  $1 \times 10^5 \text{ m}^{-3}$ .

[43] The estimated range of the upper limit of the cirrus cloud particle number concentration is at least one order of magnitude smaller than the number concentration of aerosols in the layer observed by the balloon borne OPC ( $\sim 3 \times 10^6 \text{ m}^{-3}$ , Figure 2a) at ambient temperature, and is in the same order of the concentration of nonvolatile aerosols at 200°C ( $\sim 10^5 \text{ m}^{-3}$ , Figure 2b). These results would support the suggestions by Jensen *et al.* [2010] that it is likely that the cirrus cloud particles are not formed homogeneously with the solution aerosol particles simply following the mechanism suggested by Koop *et al.* [2000], and that the clouds may be formed by solid aerosol particles (probably composed of sulfate) as ice nuclei (IN).

[44] As shown by Figure 2c, the ratio of the nonvolatile particles from the heated inlet adopted a minimum value in the upper half of the aerosol layer and adopted a low maximum in the thin cirrus layer. The coincidence of the heights of cirrus cloud and the maximum of nonvolatile particles might also support the nonvolatile solid particles working as the ice nuclei for the thin cirrus clouds. Since the sedimentation velocity of the particles with radius of 0.5  $\mu\text{m}$  is  $\sim 300 \text{ m per month}$  at 19 km in altitude [Kasten, 1968], the vertical distribution of nonvolatile particles in coarse mode ( $D_p > 0.8 \mu\text{m}$ ) that the particles distributed beneath the approximate central height of the aerosol layer (Figure 2c) could be caused by gravitational separation of the volcanic ash particles from the upper half after the volcanic eruption in late October. If there were ash particles around the aerosol layer, they would also effectively work as IN [e.g., Steinke *et al.*, 2011].

[45] The concentration of nonvolatile particles was measured by the OPC with a heated inlet, and this data provided us with information suggesting the composition of the aerosols or IN of the cirrus clouds is as described above. However, since there is no information as to whether the volatile and nonvolatile particles are mixing internally or externally, we need to be careful in interpreting the data on microphysical processes further.

### 4.3. Uncertainty of $\beta_{532}$ and CR of the Thin Cirrus Clouds Appearing in the Aerosol Layer

[46] As described in section 2.2, we assumed  $R_{532}$  at 20 km in altitude, the CR of aerosols at around 12 km in altitude, and the lidar ratios of aerosols and cirrus clouds at two wavelengths in the analysis of the lidar data in order to retrieve  $\beta_{532}$  and the CR of the thin cirrus cloud. In this

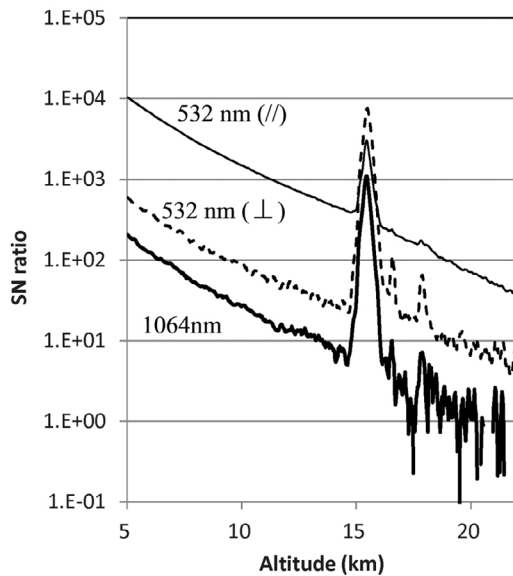


**Figure 9.** Signal to noise (SN) ratio of the lidar profiles from 03:00 to 03:05 LT on 12 January 2011 for parallel component at 532 nm (thin solid), perpendicular component at 532 nm (broken line) and at 1064 nm (bold solid). The vertical resolution of the profiles is 150 m.

section we estimate the errors caused by assuming these values and the uncertainty of the derived  $\beta_{532}$  and the CR of thin cirrus cloud that appeared in the aerosol layer. We will show the estimated error caused by background noise and the assumed values for the specific case of the observation at 03:00 LT on the 12 January. More general and analytical expressions of the error by Mie lidar observation can be found in *Russell et al.* [1979].

[47] Figure 9 depicts the signal to noise (SN) ratio of the lidar signal of the parallel (thin solid) and perpendicular (broken) polarization component at 532 nm, and of the signal at 1064 nm (bold solid) from 03:00 to 03:05 LT on 11 January. Since the statistical uncertainty of the lidar signal in our system and the case considered here is dominated by the background noise, the SN ratio is defined as the signal divided by standard deviation of the background noise. The SN ratio of the parallel component at 532 nm is larger than 10 at an altitude lower than 30 km. On the other hand the SN ratio of the signal at 1064 nm at the altitude higher than 20 km is smaller than 1. Therefore, we used the lower altitude (at around 12 km in this case) as the calibration height as mentioned in section 2.3, since the calibration at the stratospheric altitude is difficult for the data at 1064 nm. The relative error due to background noise is estimated by  $1/\text{SN}$ . The relative errors of the signal (or  $R_{532}$  and  $R_{1064}$ ) due to background noise at 532 and 1064 nm at the altitude of thin cirrus (17.8 km) are 0.5% and 14%, respectively. In the case of Figure 9 with the assumptions,  $R_{532}$  at 20 km and the CR of aerosols at around 12 km in altitudes,  $R_{532} = 1.08$  and  $R_{1064} = 1.64$  at 12 km below the cirrus clouds that are between 15 and 16 km in altitude, and  $R_{532} = 1.29$  and  $R_{1064} = 4.77$  at the altitude 17.8 km of the thin cirrus cloud. For these values, since  $\beta_{\lambda} = (R_{\lambda} - 1)\beta_{m\lambda}$ , the errors in  $\beta_{532}$  and CR caused by background noise are 2% and 17%, respectively.

[48] Although the assumption  $R_{532} = 1.10$  at around 20 km is based on the OPC observation, this value may temporally change. Although data to estimate the range of the variation over Biak is not available, since the density of the stratospheric background aerosol is usually very stable, we estimated the range of the day to day variation in  $\beta_{532}$  to be 20% in the lower stratosphere based on the observations at Lauder, New Zealand [*Nagai et al.*, 2010; T. Nagai, private communication, 2011], or this means  $R_{532} = 1.10 \pm 0.02$ . In the case above, the ranges of uncertainties of  $R_{532}$  at 12 and 17.8 km in altitude caused by this calibration are  $1.08 \pm 0.02$  and  $1.29 \pm 0.03$ , respectively. The relative errors in  $\beta_{532}$  at 12 and 17.8 km are 20% and 10%, respectively. With the assumption of CR = 1.0 at 12 km in altitude,  $R_{1064}$  equals  $1.64 \pm 0.16$  and  $4.77 \pm 0.45$  at 12 km and at 17.8 km in altitude, respectively. Then, the CR in the thin cirrus layer at 17.8 km in altitude is  $0.82 \pm 0.04$ . Therefore, the error in the CR at the altitude of the thin cirrus caused by the calibration of the signal at 532 nm is 5%.

[49] The value of the CR in the upper troposphere may change by about 10% according to the results of observations by the OPC, or CR =  $0.50 \pm 0.05$ . According to this uncertainty, the range of the CR at 17.8 km in altitude is  $0.82 \pm 0.04$ , or the error due to the calibration of 1064 nm using CR = 0.5 is 5%.

[50] The optical thickness of the aerosol alone (not including the altitudes of the cirrus clouds) when measured at 532 nm from 10 to 20 km and from 17.8 and 20 km is  $1.2 \times 10^{-2}$  and  $4.3 \times 10^{-3}$ , respectively, when using a lidar ratio of 40 sr. The two-way transmission is, respectively, 0.975 and 0.991. If we assume 35% uncertainty in the lidar ratio (or  $40 \pm 14$  sr [*Gobbi*, 1995]), the two-way transmissions included in the lidar signal from 10 to 20 km and from 17.8 to 20 km are, respectively,  $0.975 \pm 0.009$  and  $0.991 \pm 0.003$ . For the uncertainty in the lidar ratio for the aerosol, the CR and  $R_{532}$  take the values  $0.82 \pm 0.04$  and  $1.29 \pm 0.004$ . The errors in the CR and  $\beta_{532}$  at 17.8 km according to the lidar ratio of aerosol at 532 nm are 5% and 1%, respectively.

[51] The optical thickness of only by aerosol at 1064 nm from 10 to 20 km is  $1.1 \times 10^{-2}$  by using the lidar ratio of 60 sr. The two-way transmission is 0.978. If we assume a 35% uncertainty in the lidar ratio (or  $60 \pm 21$  sr), the two-way transmission included in the lidar signal from 10 to 20 km is  $0.978 \pm 0.008$ . For the uncertainty in the lidar ratio by aerosol at 1064 nm, the CR at 17.8 km takes the values  $0.82 \pm 0.002$ . The errors in the CR by lidar ratio of aerosol at 1064 nm are 0.2%.

[52] The optical thickness of the cirrus clouds alone (not including the altitudes of aerosols) at 532 nm from 10 to 20 km is  $2.2 \times 10^{-2}$  by using the lidar ratio 20 sr. The two-way transmission factor in lidar signal is 0.957. For a 50% uncertainty in the lidar ratio (or  $20 \pm 10$  sr [*Sakai et al.*, 2006]), the two-way transmission is  $0.957 \pm 0.02$ . For this lidar ratio by cirrus cloud, CR at 17.8 km takes the values  $0.82 \pm 0.2$ . The error in the CR by lidar ratio of cirrus cloud at 532 nm is 24%.

[53] Similarly at 1064 nm, the error of CR by lidar ratio of cirrus cloud at 1064 nm is 5%.

[54] In summary, the error in CR at 17.8 km is caused by the background noise (17%), the lidar ratio of cirrus cloud at 532 nm (24%), the calibration at 532 nm (5%), the

**Table 1.** Estimated Error in  $\beta_{532}$  and Color Ratio in Percent

Error Source	$\beta_{532}$	Color Ratio
Background noise	2	17
Calibration at 532 nm	10	5
Calibration at 1064 nm	...	5
Lidar ratio of aerosol at 532 nm	1	5
Lidar ratio of aerosol at 1064 nm	...	0.2
Lidar ratio of cirrus at 532 nm	...	24
Lidar ratio of cirrus at 1064 nm	...	5
Total (root-sum-square)	10	31

calibration at 1064 nm (5%), the lidar ratio of aerosol at 532 nm (5%) and at 1064 nm (0.2%), and the lidar ratio of cirrus cloud at 1064 nm (5%). If we assume these errors are independent, total error of CR is the square root of the sum of the squares (RSS) of these errors [Russell *et al.*, 1979], and is 31%.

[55] The error in  $\beta_{532}$  of thin cirrus cloud at 17.8 km in altitude is caused by calibration (10%), background noise (2%) and the lidar ratio of aerosols at 532 nm (1%). The total error (RSS) of  $\beta_{532}$  is 10%. Table 1 summarizes these estimated values. The uncertainty of our  $\beta_{532}$ , 10%, is probably small enough to know the order of the upper limit.

## 5. Summary and Conclusions

[56] Cirrus clouds, aerosols, and relative humidity around the tropical tropopause were observed by lidar, balloon borne OPC and balloon borne CFH. A stable aerosol layer around the CPT was observed throughout the survey period, and events in which cirrus cloud was formed within the aerosol layer were observed. It was shown that the aerosol layer probably originated from a volcanic eruption, and from the eruption of Merapi volcano in central Java at the end of October 2010. In the early morning on 12 January it was observed by lidar that cirrus clouds appeared in the center of the aerosol layer. Backward trajectory analysis and satellite observed equivalent blackbody temperature indicate that the cirrus cloud layer probably formed in situ within the volcanic aerosol layer. The upper limit of the number concentration of the cloud particles was estimated using lidar data and scattering theory. The estimated upper limit of the number concentration of cirrus cloud particles is more than one order of magnitude smaller than that of the aerosol particles observed by OPC at ambient temperature. These aerosol particles are volatile at the temperature 200°C, and are probably composed of liquid phase sulfuric acid and water. The upper limit is comparable to the solid particle concentration observed by OPC with 200°C heated inlet. These results are consistent with the number concentration estimated by previous studies, and support the suggested formation mechanism of cirrus cloud particles in the TTL region.

[57] If the particle size is smaller than a few micrometers, CR is a useful parameter for estimating the size of the lidar observed aerosol particles [Shibata *et al.*, 1997; Shibata and Yang, 2010]. For the particles whose size is larger than a few micrometers, CR is still useful for estimating the size if the shape of the particles is a perfect sphere as mentioned in section 4.2. But if the shape of the particles is slightly deformed from a sphere, it is difficult to use CR to estimate

size if there is no information on the shape of the particles, as was also shown in section 4.2. In those cases, if we could estimate the size by other methods or from previous studies, parameters such as the upper limit of number concentration of the particles can be estimated using the backscattering coefficient of particles, although we should be careful of the possibility that the spheroid-assumption could introduce non-negligible error in the estimation if we have no information about the shape of the ice particles.

[58] **Acknowledgments.** We acknowledge the help of LAPAN in conducting our campaign. We also acknowledge the useful comments to improve the manuscript of this paper from the three anonymous reviewers. MTSAT2 data were obtained from the Web site of Kochi University (<http://weather.is.kochi-u.ac.jp/>). This work was supported by the Japan Society for the Promotion of Science, Grant-in-Aid for Scientific Research (A) 22241004 and 21244072.

## References

- Baustian, K. J., M. E. Wise, and M. A. Tolbert (2010), Depositional ice nucleation on solid ammonium sulfate and glutaric acid particles, *Atmos. Chem. Phys.*, *10*, 2307–2317, doi:10.5194/acp-10-2307-2010.
- Brewer, A. W. (1949), Evidence for a world circulation provided by the measurements of helium and water vapour distribution in the stratosphere, *Q. J. R. Meteorol. Soc.*, *75*, 351–363, doi:10.1002/qj.49707532603.
- Carlsaw, K. S., B. Luo, and T. Peter (1995), An analytic expression for the composition of aqueous HNO<sub>3</sub>-H<sub>2</sub>SO<sub>4</sub> stratospheric aerosols including gas phase removal of HNO<sub>3</sub>, *Geophys. Res. Lett.*, *22*, 1877–1880, doi:10.1029/95GL01668.
- Chen, W. N., C. W. Chiang, and J. B. Nee (2002), The lidar ratio and depolarization ratio for cirrus clouds, *Appl. Opt.*, *41*, 6470–6476, doi:10.1364/AO.41.006470.
- Fernald, F. G. (1984), Analysis of atmospheric lidar observations: Some comments, *Appl. Opt.*, *23*, 652–653, doi:10.1364/AO.23.000652.
- Fueglistaler, S., A. E. Dessler, T. J. Dunkerton, I. Folkins, Q. Fu, and P. W. Mote (2009), Tropical tropopause layer, *Rev. Geophys.*, *47*, RG1004, doi:10.1029/2008RG000267.
- Fujiwara, M., et al. (2009), Cirrus observations in the tropical tropopause layer over the western Pacific, *J. Geophys. Res.*, *114*, D09304, doi:10.1029/2008JD011040.
- Fujiwara, M., et al. (2010), Seasonal to decadal variations of water vapor in the tropical lower stratosphere observed with balloon borne cryogenic frost point hygrometers, *J. Geophys. Res.*, *115*, D18304, doi:10.1029/2010JD014179.
- Gobbi, G. P. (1995), Lidar estimation of stratospheric aerosol properties: Surface, volume, and extinction to backscatter ratio, *J. Geophys. Res.*, *100*, 11,219–11,235, doi:10.1029/94JD03106.
- Hamada, A., and N. Nishi (2010), Development of a cloud-top height estimation method by geostationary satellite split-window measurements trained with CloudSat data, *J. Appl. Meteorol. Climatol.*, *49*, 2035–2049, doi:10.1175/2010JAMC2287.1.
- Hanson, D., and K. Mauersberger (1988), Laboratory studies of the nitric acid trihydrate: Implications for the south polar stratosphere, *Geophys. Res. Lett.*, *15*, 855–858, doi:10.1029/GL015i008p00855.
- Hasebe, F., et al. (2007), In situ observations of dehydrated air parcels advected horizontally in the tropical tropopause layer of the western Pacific, *Atmos. Chem. Phys.*, *7*, 803–813, doi:10.5194/acp-7-803-2007.
- Hayashi, M. (2001), Size distribution of aerosols in the stratosphere and troposphere observed with airborne optical particle counter (in Japanese), *Eurozoru Kenkyu*, *16*, 118–124.
- Hayashi, M., et al. (1998), Size and number concentration of liquid PSCs: Balloon-borne measurements at Ny-Alesund, Norway in winter of 1994/1995, *J. Meteorol. Soc. Jpn.*, *76*, 549–560.
- Highwood, E. J., and B. J. Hoskins (1998), The tropical tropopause, *Q. J. R. Meteorol. Soc.*, *124*, 1579–1604, doi:10.1002/qj.49712454911.
- Huffman, J. A., P. J. Ziemann, J. T. Jayne, D. R. Worsnop, and J. L. Jimenez (2008), Development and characterization of a fast-stepping/scanning thermodenuder for chemically resolved aerosol volatility measurements, *Aerosol Sci. Technol.*, *42*, 395–407, doi:10.1080/02786820802104981.
- Hurst, D. F., et al. (2011), Stratospheric water vapor trends over Boulder, Colorado: Analysis of the 30 year Boulder record, *J. Geophys. Res.*, *116*, D02306, doi:10.1029/2010JD015065.
- Iwasaki, S., et al. (2007), Characteristics of aerosol and cloud particle size distributions in the tropical tropopause layer measured with optical particle counter and lidar, *Atmos. Chem. Phys.*, *7*, 3507–3518, doi:10.5194/acp-7-3507-2007.

- Iwasaki, S., T. Shibata, J. Nakamoto, H. Okamoto, H. Ishimoto, and H. Kubota (2010), Characteristics of deep convection measured by using the A-train constellation, *J. Geophys. Res.*, *115*, D06207, doi:10.1029/2009JD013000.
- Jensen, E. J., and O. B. Toon (1992), The potential effects of volcanic aerosols on cirrus clouds microphysics, *Geophys. Res. Lett.*, *19*, 1759–1762, doi:10.1029/92GL01936.
- Jensen, E. J., L. Pfister, T.-P. Bui, P. Lawson, and D. Baumgardner (2010), Ice nucleation and cloud microphysical properties in tropical tropopause layer cirrus, *Atmos. Chem. Phys.*, *10*, 1369–1384, doi:10.5194/acp-10-1369-2010.
- Kasten, F. (1968), Falling speed of aerosol particles, *J. Appl. Meteorol.*, *7*, 944–947, doi:10.1175/1520-0450(1968)007<0944:FSOAP>2.0.CO;2.
- Koop, T., B. Luo, A. Tsias, and T. Peter (2000), Water activity as the determinant for homogeneous ice nucleation in aqueous solutions, *Nature*, *406*, 611–614, doi:10.1038/35020537.
- Krämer, M., et al. (2009), Ice supersaturations and cirrus cloud crystal numbers, *Atmos. Chem. Phys.*, *9*, 3505–3522, doi:10.5194/acp-9-3505-2009.
- Lawson, R. P., B. Pilon, B. Baker, Q. Mo, E. Jensen, L. Pfister, and P. Bui (2008), Aircraft measurements of microphysical properties of subvisible cirrus in the tropical tropopause layer, *Atmos. Chem. Phys.*, *8*, 1609–1620, doi:10.5194/acp-8-1609-2008.
- Mishchenko, M. I., and L. D. Travis (1998), Capabilities and limitations of a current FORTRAN implementation of the T-matrix method for randomly oriented, rotationally symmetric scatterers, *J. Quant. Spectrosc. Radiat. Transfer*, *60*, 309–324, doi:10.1016/S0022-4073(98)00008-9.
- Murray, B. J., D. A. Knopf, and A. K. Bertram (2005), The formation of cubic ice under conditions relevant to Earth's atmosphere, *Nature*, *434*, 202–205, doi:10.1038/nature03403.
- Nagai, T., B. Liley, T. Sakai, T. Shibata, and O. Uchino (2010), Post-Pinatubo evolution and subsequent trend of the stratospheric aerosol layer observed by mid-latitude lidars in both hemispheres, *SOLA*, *6*, 69–72, doi:10.2151/sola.2010-018.
- Oltmans, S. J., and D. J. Hofmann (1995), Increase in lower-stratospheric water vapour at a mid-latitude Northern Hemisphere site from 1981 to 1994, *Nature*, *374*, 146–149, doi:10.1038/374146a0.
- Peter, T., et al. (2003), Ultrathin tropical tropopause clouds (UTTCs): I. cloud morphology and occurrence, *Atmos. Chem. Phys.*, *3*, 1083–1091, doi:10.5194/acp-3-1083-2003.
- Pruppacher, H. R., and J. D. Klett (1978), *Microphysics of Clouds and Precipitation*, Springer, New York, doi:10.1007/978-94-009-9905-3.
- Rosen, J. M. (1971), The boiling point of stratospheric aerosols, *J. Appl. Meteorol.*, *10*, 1044–1046, doi:10.1175/1520-0450(1971)010<1044:TBPOSA>2.0.CO;2.
- Russell, P. B., T. J. Swisler, and M. P. McCormick (1979), Methodology for error analysis and simulation of lidar aerosol measurements, *Appl. Opt.*, *18*, 3783–3797.
- Sakai, T., et al. (2006), Optical and microphysical properties of upper clouds measured with the Raman lidar and hydrometeor videonode: A case study on 29 March 2004 over Tsukuba, Japan, *J. Atmos. Sci.*, *63*, 2156–2166, doi:10.1175/JAS3736.1.
- Sassen, K. (1992), Evidence for liquid-phase cirrus cloud formation from volcanic aerosols: Climatic implications, *Science*, *257*, 516–519, doi:10.1126/science.257.5069.516.
- Schmetz, J., S. A. Tjemkes, M. Gube, and L. van de Berg (1997), Monitoring deep convection and convective overshooting with METEOSAT, *Adv. Space Res.*, *19*(3), 433–441, doi:10.1016/S0273-1177(97)00051-3.
- Shibata, T., and T. Kouketsu (2008), Volcanic clouds from the 2007 eruption of Jebel at Tair (Yemen) detected by ground based and space borne lidar, *SOLA*, *4*, 93–96, doi:10.2151/sola.2008-024.
- Shibata, T., and Y. Yang (2010), Decrease in depolarization of dust over populated areas of eastern Asia observed by the space-borne lidar CALIOP, *Eurozoru Kenkyu*, *25*, 62–76.
- Shibata, T., Y. Iwasaka, M. Fujiwara, M. Hayashi, M. Nagatani, K. Shiraishi, H. Adachi, T. Sakai, K. Susumu, and Y. Nakura (1997), Polar stratospheric clouds observed by lidar over Spitsbergen in the winter 1994/1995: Liquid particles and vertical “sandwich” structure, *J. Geophys. Res.*, *102*, 10,829–10,840, doi:10.1029/97JD00418.
- Shibata, T., K. Shiraishi, H. Adachi, Y. Iwasaka, and M. Fujiwara (1999), On the lidar-observed sandwich structure of polar stratospheric clouds (PSCs): I. Implications for the mixing state of the PSC particles, *J. Geophys. Res.*, *104*, 21,603–21,611, doi:10.1029/1999JD900333.
- Shibata, T., et al. (2007), Tropical cirrus clouds near cold point tropopause under ice supersaturated conditions observed by lidar and balloon-borne cryogenic frost point hygrometer, *J. Geophys. Res.*, *112*, D03210, doi:10.1029/2006JD007361.
- Solomon, S., K. Rosenlof, R. Portmann, J. Daniel, S. Davis, T. Sanford, and G.-K. Plattner (2010), Contributions of stratospheric water vapor to decadal changes in the rate of global warming, *Science*, *327*, 1219–1223, doi:10.1126/science.1182488.
- Steinke, I., O. Möhler, A. Kiselev, M. Niemand, H. Saathoff, M. Schnaiter, J. Skrotzki, C. Hoose, and T. Leisner (2011), Ice nucleation properties of fine ash particles from the Eyjafjallajökull eruption in April 2010, *Atmos. Chem. Phys.*, *11*, 12,945–12,958, doi:10.5194/acp-11-12945-2011.
- Tabazadeh, A., R. P. Turco, and M. Z. Jacobson (1994), A model for studying the composition and chemical effects of stratospheric aerosols, *J. Geophys. Res.*, *99*, 12,897–12,914, doi:10.1029/94JD00820.
- Vaughan, M. A., Z. Liu, M. J. McGill, Y. Hu, and M. D. Obland (2010), On the spectral dependence of backscatter from cirrus clouds: Assessing CALIOP's 1064 nm calibration assumptions using cloud physics lidar measurements, *J. Geophys. Res.*, *115*, D14206, doi:10.1029/2009JD013086.
- Vernier, J. P., et al. (2009), Tropical stratospheric aerosol layer from CALIPSO lidar observations, *J. Geophys. Res.*, *114*, D00H10, doi:10.1029/2009JD011946.
- Vömel, H., D. E. David, and K. Smith (2007), Accuracy of tropospheric and stratospheric water vapor measurements by the cryogenic frost point hygrometer instrumental details and observations, *J. Geophys. Res.*, *112*, D08305, doi:10.1029/2006JD007224.
- Warren, S. G. (1984), Optical constants of ice from the ultraviolet to the microwave, *Appl. Opt.*, *23*, 1206–1225, doi:10.1364/AO.23.001206.
- Wise, M. E., K. J. Baustian, and M. A. Tolbert (2010), Internally mixed sulfate and organic particles as potential ice nuclei in the tropical tropopause region, *Proc. Natl. Acad. Sci. U. S. A.*, *107*, 6693–6698, doi:10.1073/pnas.0913018107.
- Zobrist, B., C. Macolli, D. A. Pedernera, and T. Koop (2008), Do atmospheric aerosols form glasses?, *Atmos. Chem. Phys.*, *8*, 5221–5244, doi:10.5194/acp-8-5221-2008.